



Dual redox couples Ag/Ag^+ and $\text{I}^-/(\text{IO}_3)^-$ self-sacrificed transformation for realizing multiplex hierarchical architectures with universally powerful photocatalytic performance



Chao Zeng^a, Hongwei Huang^{a,*}, Fan Dong^b, Liqun Ye^c, Tierui Zhang^d, Yihe Zhang^a,
Yuxi Guo^a, Chengyin Liu^a, Yingmo Hu^{a,*}

^a Beijing Key Laboratory of Materials Utilization of Nonmetallic Minerals and Solid Wastes, National Laboratory of Mineral Materials, School of Materials Science and Technology, China University of Geosciences, Beijing 100083, China

^b Chongqing Key Laboratory of Catalysis and Functional Organic Molecules, College of Environmental and Biological Engineering, Chongqing Technology and Business University, Chongqing, 400067, China

^c Key Laboratory of Ecological Security for Water Source Region of Mid-line Project of South-to-North Water Diversion of Henan Province, College of Chemistry and Pharmaceutical Engineering, Nanyang Normal University, Nanyang 473061, China

^d Key Laboratory of Photochemical Conversion and Optoelectronic Materials, Technical Institute of Physics and Chemistry, Chinese Academy of Sciences, Beijing 100190, China

ARTICLE INFO

Article history:

Received 9 June 2016

Received in revised form 17 July 2016

Accepted 18 July 2016

Available online 19 July 2016

Keywords:

Heterostructural photocatalyst

Photocatalysis

SPR

$\text{Ag}-\text{AgI}-\text{AgIO}_3$

Reduction reaction

ABSTRACT

Utilizing self-sacrificed transformation of the dual redox couples Ag/Ag^+ and $\text{I}^-/(\text{IO}_3)^-$, we developed a multiplex heterostructure $\text{Ag}-\text{AgI}-\text{AgIO}_3$ by using a simple in-situ reduction strategy and AgIO_3 as the sacrificed template. The reaction extent can be easily controlled via adjusting the reductant NaBH_4 concentration. Benefiting from both Ag SPR and heterojunctional effects, the photoabsorption in the UV-vis region of $\text{Ag}-\text{AgI}-\text{AgIO}_3$ is monotonously enhanced with increasing reductant concentration. The composite photocatalysts all exhibit highly enhanced photocatalytic activity in degrading methyl orange (MO) under both UV light and visible light irradiation, and $\text{Ag}-\text{AgI}-\text{AgIO}_3-5$ sample shows the optimal photoreactivity, which is 15.2 times that of pure AgIO_3 . Notably, it also possesses unsurpassed photocatalytic activity against diverse industrial contaminants, pharmaceuticals, and gaseous NO. Besides, $\text{Ag}-\text{AgI}-\text{AgIO}_3-5$ also displays better photocatalytic performance in converting CO_2 to CO than AgIO_3 . Particularly, we explore the reduction products of AgIO_3 by other different reductants. It is fascinating that the introduction of sodium citrate, thiourea and hydrazine hydrate results in the products $\text{Ag}-\text{AgIO}_3$, $\text{AgI}-\text{AgIO}_3$, $\text{Ag}-\text{AgI}-\text{AgIO}_3$ composites, respectively. This work may not only offer a universally powerful and stable photocatalyst for environmental and energy applications, but also open up a new avenue to develop component-adjustable polynary heterostructural photocatalysts in a facile way.

© 2016 Elsevier B.V. All rights reserved.

1. Introduction

Semiconductor-based photocatalysts have gained considerable attention due to their superior abilities for environmental remediation and energy conversion [1,2]. Wide-band-gap (WBG) semiconductors, of which energy band potentials are further away from the Fermi level, always possess strong oxidation and reduction power. Whereas, these WBG semiconductors only can be excited by UV (ultraviolet) light, which accounts for 4% of solar spectrum

[3]. Currently, to harness visible light (~48% of the solar spectrum), many attempts have been paid to enhance the visible light response of WBG semiconductors, such as, element doping, fabrication of heterojunctions, and noble metal deposition, etc [4–6]. Among them, fabrication of a heterostructure and noble metal (Au, Pt, Ag) deposition can strengthen visible-light response and facilitate the separation of photoinduced charges of semiconductors [7,8]. However, introducing foreign noble metal or semiconductor would lead to undesirable thermal and chemical instability. Therefore, it is of great significance and challenge to build a structure which combines a heterojunction and noble metal via components transformation from the self-sacrifice precursor template [9,10].

Benefiting from multi-factor synergism, including excellent transfer efficiency of photoinduced charges and good light absorp-

* Corresponding authors.

E-mail addresses: hhw@cugb.edu.cn (H. Huang), huyingmo@cugb.edu.cn (Y. Hu).



Scheme 1. Schematic illustration for fabrication of pure AgI0_3 and $\text{Ag}-\text{AgI}-\text{AgI0}_3$ composites photocatalysts (the number in the right picture means $\text{NaBH}_4/\text{AgI0}_3$ molar ratios).

tion, multiple heterostructural photocatalysts always exhibit outstanding photocatalytic activity [11,12]. For example, $\text{Ag}-\text{Ag}_3\text{PO}_4-\text{g-C}_3\text{N}_4$, reported by Yang et al., exhibits great oxygen activity of 19 $\mu\text{mol}/\text{L}$ in 14 min [13]. Besides, Li et al. synthesize $\text{WO}_3-\text{Ag}-\text{C}_3\text{N}_4$ composite photocatalyst, which shows unprecedented photocatalysis performance in photodegrading 4-nonylphenol [14]. However, heterostructural photocatalysts with multiple active components, stuck with the tedious preparation process, cannot be widely applied [15,16]. Accordingly, multiplex heterostructure photocatalysts synthesized by one-pot facile method would arouse tremendous sensation.

Recently, benefiting from lone pair electrons of I^{5+} in IO_3 group, which is conducive to the formation of asymmetry structure and polarity, the metal iodates possess superior photographic activity for removal azo dye, 2,4-Dichlorophenol and Hg^{2+} under UV light irradiation [17–19]. On the other hand, semiconductors with especial $\text{d}^{10}/\text{d}^{10}\text{s}^2$ metal ion Ag^+ shows superior photocatalytic performance, because Ag cation can enhance the valence band and modestly narrow the band gap of the semiconductor [20]. Thereby, as reported in previous papers, AgI0_3 [21,22], a new photocatalyst with a large band gap (~ 3.2 eV), possesses benign capacity to remove liquid contaminant and convert CO_2 to CH_4 and CO under UV light. But AgI0_3 exhibits weak visible-light absorption. To improve the utilization of solar energy, designing high-performance AgI0_3 -based heterojunctions is necessary and significant. Nowadays, the silver halide AgX ($\text{X}=\text{Cl}, \text{Br}, \text{I}$) is well known due to its prominent response to visible light and eminent photocatalytic activity for photodecolorizing azo dyes [23,24]. Wherein, yellow colored semiconductors silver iodates (AgI) is a relative narrow-band-gap (NBG) photocatalyst with a band gap of ~ 2.8 eV, which can be used as an efficient photosensitizer to improve the light absorption of WBG photocatalyst [25]. What is more, Ag nanoparticles show strong visible light absorption on account of the surface plasmon resonance (SPR) of metallic Ag species. For example, Ag/TiO_2 plasmonic photocatalyst possesses appreciable photocatalytic property for photodegrading gaseous acetone under excitation of visible light [26]. Ag/BiOCl exhibits efficient photocatalytic activity under visible light illumination [27]. Therefore, AgI and Ag SPR effect may be together used to expand AgI0_3 light absorption and promote its visible-light-induced photocatalytic activity.

In this article, based on the two types of redox couples (IO_3^-/I^- and Ag/Ag^+ in AgI0_3), we fabricate $\text{Ag}-\text{AgI}-\text{AgI0}_3$ ternary heterostructure photocatalyst via a facile *in-situ* reduction method taking sodium borohydride (NaBH_4) as reductant to react with AgI0_3 . The $(\text{IO}_3)^-$ and Ag^+ ions can be separately reduced to be I^- and Ag , and then AgI and Ag particles are generated on the surface of AgI0_3 . All the $\text{Ag}-\text{AgI}-\text{AgI0}_3$ composite photocatalysts exhibit much higher photocatalytic activity than the pristine AgI0_3 in photodegradation of methyl orange (MO) under the irradiation of both UV light and visible light ($\lambda > 420$ nm). Meanwhile, the different photocatalytic mechanisms corresponding to different light source are investigated systematically. Amazingly, the as-obtained

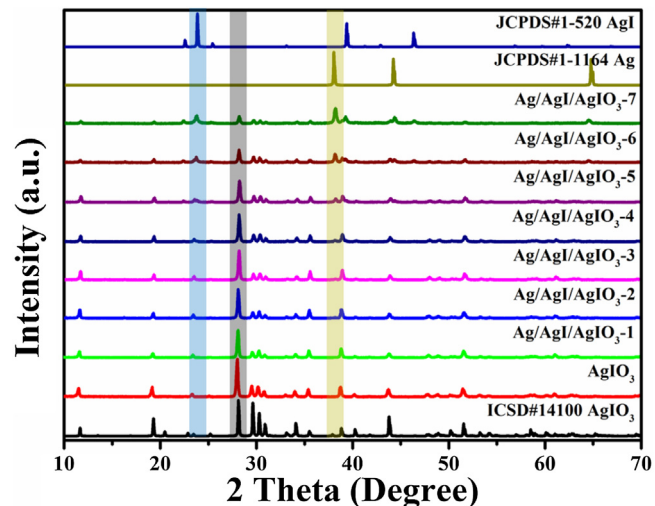


Fig. 1. XRD patterns of pure AgI0_3 sample, and $\text{Ag}-\text{AgI}-\text{AgI0}_3$ composite photocatalysts.

composite photocatalyst also shows noteworthy photocatalytic activity in decomposition of diverse industrial contaminants and pharmaceuticals, such as rhodamine B (RhB), 2,4-Dichlorophenol (2,4-DCP), phenol, chlortetracycline hydrochloride, tetracycline hydrochloride, bisphenol A (BPA), diclofenac sodium and NO in gaseous phase under visible light illumination. Besides, we explore the reduction products of AgI0_3 using other different reductants and interestingly find that different composite photocatalysts, including $\text{Ag}-\text{AgI0}_3$, $\text{AgI}-\text{AgI0}_3$ and $\text{Ag}-\text{AgI}-\text{AgI0}_3$, can be separately obtained. This research perhaps sheds new light on fabrication of high-performance multiplex heterostructural photocatalysts.

2. Experimental section

2.1. Preparation of the photocatalyst

All the reagents used here are analytical grade. AgI0_3 precursor was fabricated by a hydrolysis method. In a typical synthesis, 1 mmol I_2O_5 and 2 mmol AgNO_3 were dissolved in 15 mL of deionized water, respectively, and then these aqueous solutions were of ultrasonic to form a homogeneous suspension. Under magnetic agitation, the aqueous solution of I_2O_5 was dropwise added into the AgNO_3 solution. After stirring for 30 min at room temperature, the white precipitate was collected by filtration, washed, and dried at 60°C overnight in air.

The $\text{Ag}-\text{AgI}-\text{AgI0}_3$ composites photocatalysts were synthesized by a facile *in-situ* reduction reaction. Representatively, 0.6 g AgI0_3 powder was ultrasonically dispersed into 20 mL of deionized water. Then, 20 mL NaBH_4 solution with different $\text{NaBH}_4/\text{AgI0}_3$ molar ratios of 0.5%, 2%, 5%, 10%, 20%, 40%, and 60% was added into the AgI0_3 sus-

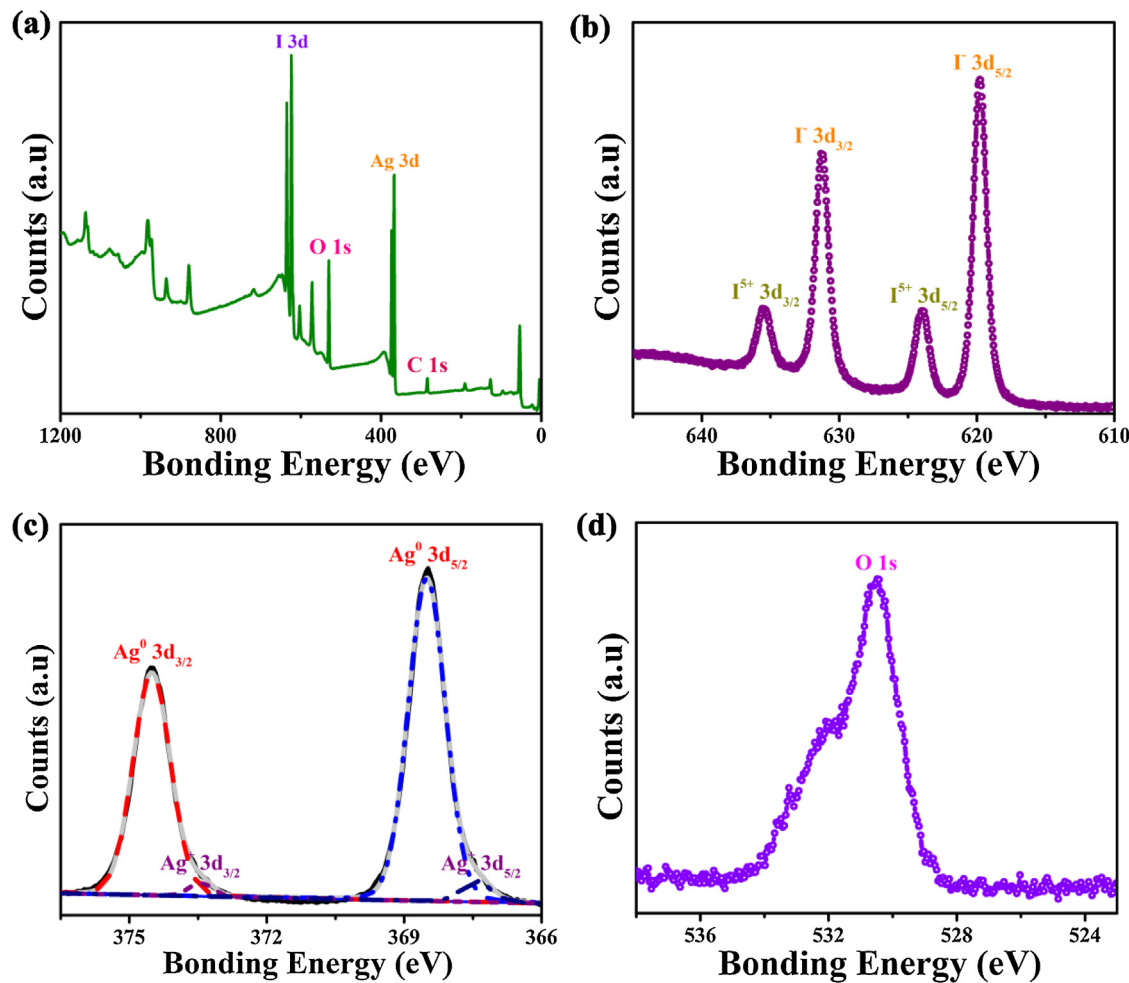


Fig. 2. XPS spectra of Ag-Agl-AgI03-5 composite photocatalyst (a), high-resolution XPS spectrum for I 3d (b), Ag 3d (c), and O 1s (d).

pension under stirring drop by drop. After strong stirring for 1 h at room temperature, the products were filtrated, washed with distilled water and ethanol for three times, and dried at 60 °C overnight. The composite photocatalysts with different NaBH₄ concentration (NaBH₄/AgI0₃ = 0.5%, 2%, 5%, 10%, 20%, 40%, and 60%) were marked as Ag-Agl-AgI0₃-1, Ag-Agl-AgI0₃-2, Ag-Agl-AgI0₃-3, Ag-Agl-AgI0₃-4, Ag-Agl-AgI0₃-5, Ag-Agl-AgI0₃-6, and Ag-Agl-AgI0₃-7, respectively. The schematic illustration for the preparation process of the composite samples was depicted in **Scheme 1**. Other reduction reactions were operated with the same method just substituting NaBH₄ with sodium citrate, thiourea, and hydrazine hydrate, respectively.

2.2. Characterization

X-ray powder diffraction (XRD) was conducted using a Bruker D8 focus with Cu K α radiation (40 kV/40 mA). X-ray photoelectron spectroscopy (XPS) was measured by an ESCALAB 250xi (ThermoFisher, England) electron spectrometer. Scanning electron microscopy (SEM) and transmission electron microscopy (TEM) were performed on Hitachi S-4800 and JEM-2100 to study the morphologies and microstructure of the as-prepared photocatalysts. UV-vis diffuse reflectance spectra (DRS) were recorded on a Varian Cary 5000 UV-vis spectrophotometer. The photoluminescence (PL) spectra was carried out on a Hitachi F-4600 fluorescence spectrophotometer using a xenon lamp as an excitation light source. All the measurements were measured at room temperature.

2.3. Photocatalytic activity

2.3.1. Photodegrading diverse liquid pollutants

The photocatalytic performance of as-synthesized composites photocatalysts was assessed by photocatalytic degradation of various industrial pollutants, including the organic dye pollutants rhodamine B (RhB, 5*10⁻⁶ mol/L), methyl orange (MO, 5*10⁻⁶ mol/L), bisphenol A (BPA, 5 mg/L), 2,4-dichlorophenol (2,4-DCP, 5 mg/L), phenol (5 mg/L), and pharmaceuticals tetracycline hydrochloride (10 mg/L), chlortetracycline hydrochloride (10 mg/L), diclofenac sodium (10 mg/L), under UV light or visible light ($\lambda > 420$ nm) illumination. 20 mg photocatalyst powder was adequately suspended in 40 mL of pollutant aqueous solution. Prior to irradiation, the mixtures were vigorously stirred in dark for 30 min to reach an adsorption-desorption equilibrium between aqueous solution and catalyst. After irradiation, at a certain period time, 3 mL of suspension was sampled from each quartz tube, and centrifuged to remove the precipitate. The concentration and temporal absorption spectra of the supernatant liquid was analyzed and obtained by recording the absorbance between 200 and 800 nm on a Cary 5000 UV-vis spectrophotometer.

2.3.2. Photodegrading diverse gaseous pollutant NO

The photocatalytic activity was also evaluated by removal of NO at ppb levels at ambient temperature. A commercial tungsten halogen lamp (150 W) was taken as light source. A 420 nm cutoff filter was used to remove UV light in the light beam. A total of 150 mg

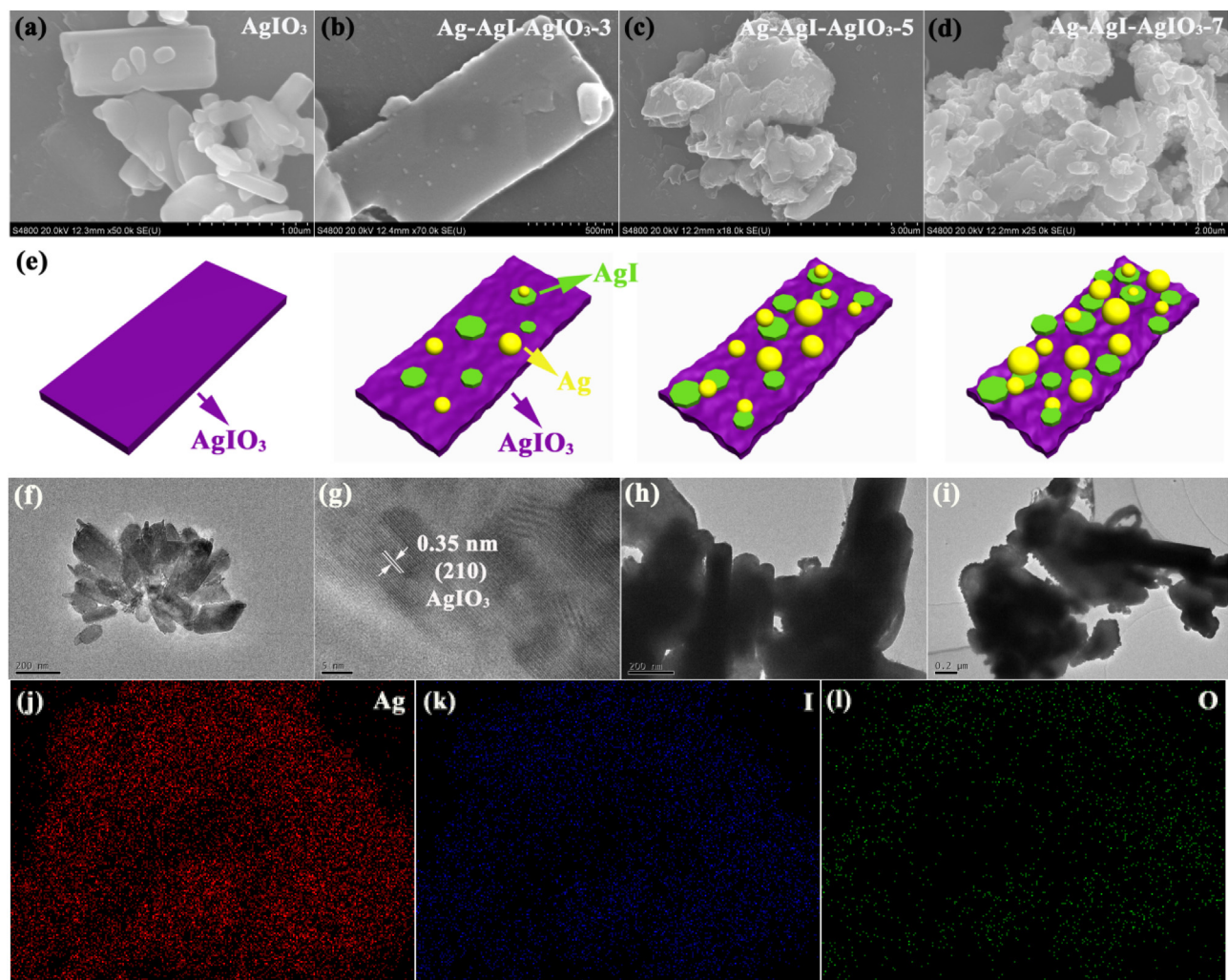


Fig. 3. SEM images for AgIO_3 (a), $\text{Ag}-\text{AgI}-\text{AgI}-\text{AgO}_3$ -3 (b), $\text{Ag}-\text{AgI}-\text{AgI}-\text{AgO}_3$ -5 (c), $\text{Ag}-\text{AgI}-\text{AgI}-\text{AgO}_3$ -7 (d), Schematic illustration of morphology changes for AgIO_3 , $\text{Ag}-\text{AgI}-\text{AgI}-\text{AgO}_3$ -3, $\text{Ag}-\text{AgI}-\text{AgI}-\text{AgO}_3$ -5, and $\text{Ag}-\text{AgI}-\text{AgI}-\text{AgO}_3$ -7 products (e), TEM (f) and HRTEM (g) images of AgIO_3 sample, TEM images of $\text{Ag}-\text{AgI}-\text{AgI}-\text{AgO}_3$ -5 sample (h–i), EDX mapping of $\text{Ag}-\text{AgI}-\text{AgI}-\text{AgO}_3$ -5 (j–l).

photocatalyst was suspended in 50 mL of deionized water. With ultrasonic treatment of 10 min, the suspension was coated onto a dish (12.0 cm in diameter). Then, the coated dish was preprocessed at 60 °C to remove water in the suspension. The necessary 450 ppb NO gas in the measurement was obtained via diluting 100 ppm NO gas from a compressed gas cylinder with an air stream. After achieving adsorption-desorption equilibrium, the concentrations of NO_x (NO and NO_2) were recorded by a NO_x analyzer (Thermo Scientific, 42i-TL), and the concentration of NO was determined.

2.3.3. Photoreduction CO_2 to CO

The CO_2 photoreduction experiment was performed by a PLS-SXE300 Labsolar-IIIAG closed gas system (Perfectlight Technology Co., China). The total volume for the reaction was 500 mL. A total of 50 mg photocatalyst was evenly suspended on a watch glass, of which the area was about 28 cm^2 . Then, 1.712 g of NaHCO_3 reagent was added into the reactor followed with exhaustive vacuum treatment to remove air. Before photoreaction, H_2SO_4 (4 M, 5 mL) was added into the cell to react with NaHCO_3 and got 1 atm CO_2 gas. Subsequently, the reactor was illuminated by 300 W high pressure xenon lamp (PLS-SXE300, Beijing Perfect light Technology Co. Ltd. China), and the temperature in the reactor was kept at 20 °C with DC-0506 low-temperature thermostat bath (Sunny Hengping Scientific Instrument Co., Ltd., China). At certain time intervals, 1 mL

of the resulting gas was collected and then qualitatively analyzed by a GC9790II gas chromatograph (Zhejiang Fuli Analytical Instrument Co., Ltd., China) equipped with a flame ionization detector (FID, GDX502 columns). The outlet gases were determined to be CO_2 , CO , and CH_4 . The production yield was calculated on the basis of a calibration curve.

2.4. Active species trapping experiment

There are several kinds of active species that would generate in the photocatalytic process, including hydroxyl radical ($\cdot\text{OH}$), hole (h^+), and superoxide radical ($\cdot\text{O}_2^-$). To identify the active species produced during the photocatalytic process of MO, another MO photodegradation experiment was conducted with adding 1 mM benzoquinone (BQ), 1 mM disodium ethylenediaminetetraacetate (EDTA-2Na) and 1 mM ethylene glycol (IPA) to scavenge $\cdot\text{O}_2^-$, h^+ , and $\cdot\text{OH}$, respectively.

2.5. Photoelectrochemical measurement

The Mott–Schottky curve was carried out on an electrochemical analyzer (CHI660E, Shanghai), which was equipped with a standard three-electrode system. The counter electrode was a platinum (Pt) wire and reference electrode was saturated calomel electrodes

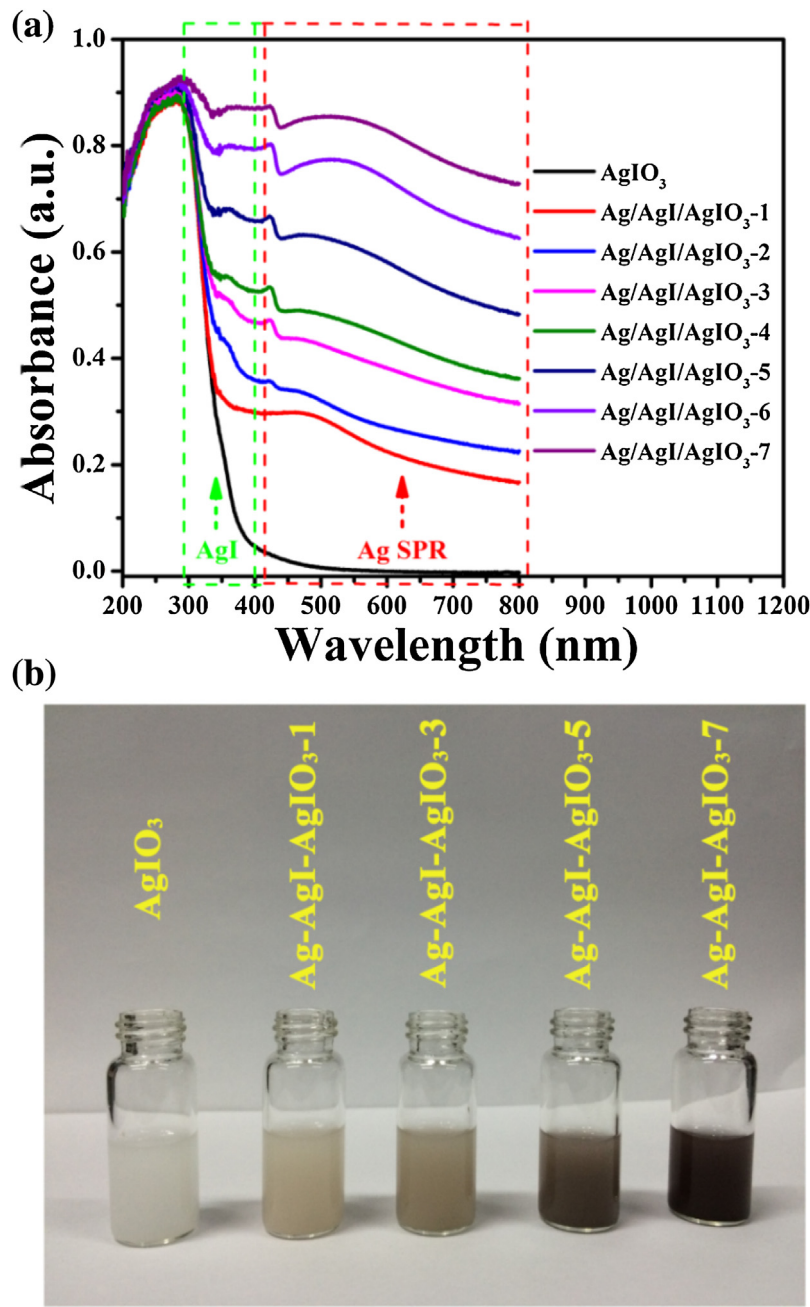


Fig. 4. DRS spectra (a) and digital photos of suspensions (b) for the AgI_3 , and $\text{Ag}/\text{AgI}/\text{AgI}_3$ composite photocatalysts.

(SCE). A 300 W Xe arc lamp (without filter) was used as light source. Na_2SO_4 (0.1 M) aqueous solution worked as an electrolyte solution. The working electrode was the AgI_3 , and $\text{Ag}/\text{AgI}/\text{AgI}_3$ -5 sample films coated on ITO.

3. Results and discussion

3.1. Structure and morphology

Fig. 1 displays the XRD patterns of the as-obtained pure AgI_3 sample, and $\text{Ag}/\text{AgI}/\text{AgI}_3$ composite photocatalysts. All the diffraction peaks of AgI_3 precursor are identical to the AgI_3 standard card (ICSD # 14100). With introducing NaBH_4 into AgI_3 suspension, there are obvious changes in the XRD patterns of products from reduction reaction, revealing the formation of new

phases. On the basis of the standard dates of AgI_3 (ICSD # 14100), AgI (JCPDS # 1-520), and Ag (JCPDS # 1-1164), the as-prepared composite samples consist of $\text{Ag}/\text{AgI}/\text{AgI}_3$ three phases. The diffraction peaks centered at about 28.1° , 23.9° , and 37.9° are assigned to AgI_3 , AgI , and Ag phases, respectively, which are emphasized by gray, blue, and cameo brown tapes. With increasing the concentration of NaBH_4 , the intensity of peaks for AgI_3 declines, and simultaneously the intensity of peaks for AgI and Ag ascends, which evidences the conversion from AgI_3 to AgI and Ag through the reduction reaction between AgI_3 and NaBH_4 . Accordingly, the fabrication of $\text{Ag}/\text{AgI}/\text{AgI}_3$ multiplex heterostructure photocatalyst via one-pot in-situ reaction is realized.

The X-ray photoelectron spectroscopy (XPS) of $\text{Ag}/\text{AgI}/\text{AgI}_3$ -5 sample is carried out to analyze its element composition and chemical status. It can be observed from Fig. 2(a) that the $\text{Ag}/\text{AgI}/\text{AgI}_3$ -5

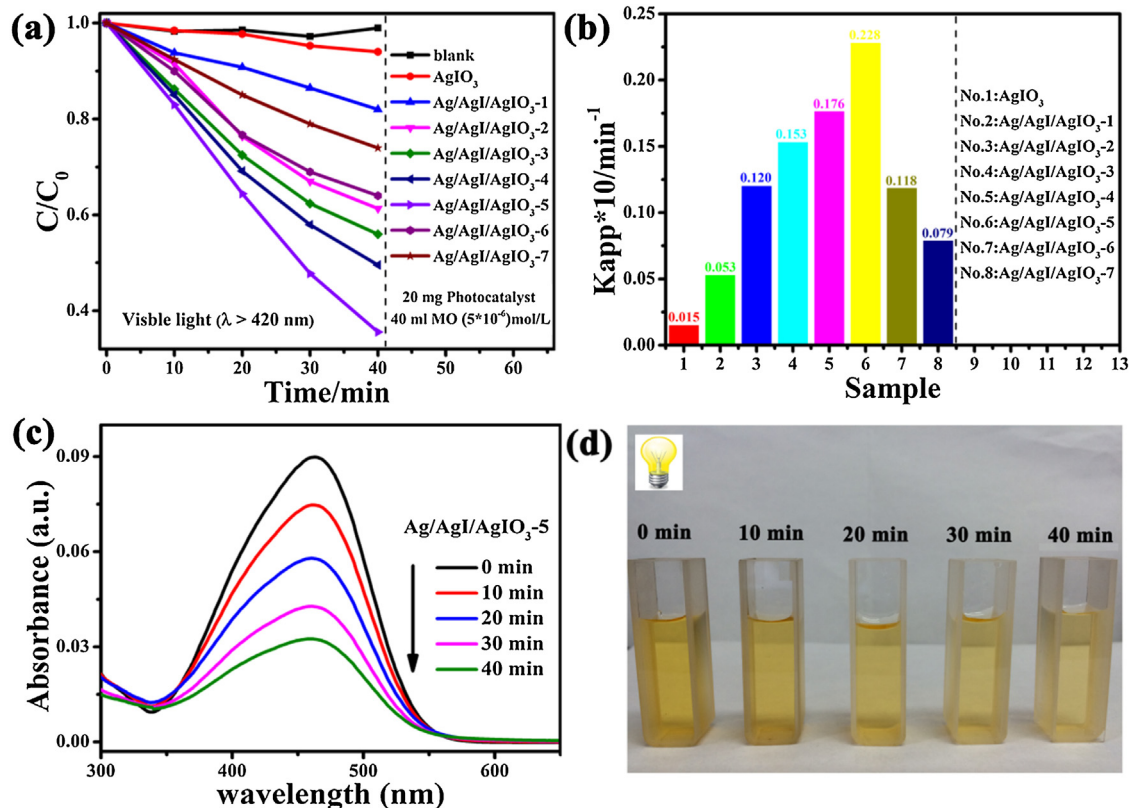


Fig. 5. Photocatalytic degradation curves of MO over the AgI03 precursor and Ag-AgI-AgI03 composite photocatalysts under visible light ($\lambda > 420$ nm) illumination (a), apparent rate constants for degrading MO over AgI03, and Ag-AgI-AgI03 samples (b), temporal absorption spectra patterns of MO (c) and color change of MO solution (d) over Ag-AgI-AgI03-5 sample (for interpretation of the references to colour in this figure legend, the reader is referred to the web version of this article).

composite photocatalyst is composed of Ag, I, and O atoms. The XPS peak for C 1s (locates at about 284.8 eV) is assigned to the residual hydrocarbon from the XPS instrument. The high-resolution XPS spectrum for I 3d is displayed in Fig. 2(b). Four peaks centering at 619.7, 623.8, 631.2 and 635.4 eV can be ascribed to I^- 3d_{5/2}, I^{5+} 3d_{5/2}, I^- 3d_{3/2}, and I^{5+} 3d_{3/2}, respectively, suggesting that there are two kinds of chemical states (I^- and I^{5+}) for I element [28]. Fig. 2(c) shows the high-resolution XPS spectrum for Ag 3d, and its spectrum can be deconvoluted into two sets of bands. Two peaks at 373.4 eV and 367.4 eV match the features of Ag^+ 3d_{3/2} and Ag^+ 3d_{5/2}, and meantime the peaks at 374.5 eV and 368.5 eV can be assigned to Ag^0 3d_{3/2} and Ag^0 3d_{5/2}, respectively [29,30]. This result corroborates the co-existence of Ag^+ and Ag^0 . The high-resolution XPS spectrum for O 1s is exhibited in Fig. 2(d). The peak for O 1s locates at about 530.5 eV [31]. The XPS results further support that there are Ag, AgI, and AgI03 three phases in the composite photocatalyst, which is consistent with XRD results.

To investigate morphology and microstructure of the as-synthesized photocatalysts, scanning electron microscopy (SEM), transmission electron microscopy (TEM), high-resolution TEM (HRTEM), and EDX mapping are performed and shown in Fig. 3. As observed from Fig. 3(a-d), pure AgI03 products are rectangular sheets with a diameter of 1–10 μm . Upon introducing NaBH4 into AgI03 suspension, the surface of AgI03 becomes rough. Meanwhile, some nanosheets and nanoparticles emerge on the surface of AgI03, which can be attributed to be AgI and Ag, respectively. With increasing the concentration of NaBH4, the surface of AgI03 is getting rougher, in the meantime, more AgI nanosheets and Ag nanoparticles generate. In Fig. 3(e), the schematic illustration clearly shows the morphology changes of AgI03, Ag-AgI-AgI03-3, Ag-AgI-AgI03-5, and Ag-AgI-AgI03-7 samples. The TEM image of

AgI03 (Fig. 3(f)) further confirms the AgI03 sheet with a smooth surface. As shown in Fig. 3(g), the sole lattice fringe with a distance of 0.35 nm coincides with the (210) facet of AgI03. TEM images of Ag-AgI-AgI03-5 sample are exhibited in Fig. 3(h-i). Some nanoparticles, which may be Ag species, are found at the edge of sheets. Owing to the instability of AgI under electron beam irradiation [32], its crystal lattice cannot be observed. Furthermore, EDX mapping (Fig. 3(j-l)) indicates that the uniform distribution of Ag, I, and O elements in Ag-AgI-AgI03-5 sample.

3.2. Light absorption adjusting

Diffuse reflection spectroscopy (DRS) is performed to investigate the optical property of the as-prepared photocatalysts. As shown in Fig. 4(a), the absorption edge of AgI03 is located at approximately 371 nm, corresponding to a photonic energy band gap of 3.34 eV [22]. Compared with the AgI03 precursor, the Ag-AgI-AgI03 composite photocatalysts exhibit enhanced light response in both ultraviolet and visible regions. The photoresponse enhancement in the UV region (300–400 nm) is mainly due to the generation of AgI. On the other hand, light harvesting ability in visible region of composite photocatalysts is improved because of the strong SPR effect of Ag nanocrystals distributed on the surface of samples. With increasing the concentration of NaBH4, the light absorption in UV-vis region (300–800 nm) of Ag-AgI-AgI03 composite photocatalysts is continuously strengthened, which is in line with the color changes from white to black of sample suspensions (Fig. 4(b)). Therefore, the generation of Ag and I^- species from the self-sacrificed AgI03 production of Ag-AgI can effectively enhance the light absorption of the WBG semiconductors AgI03.

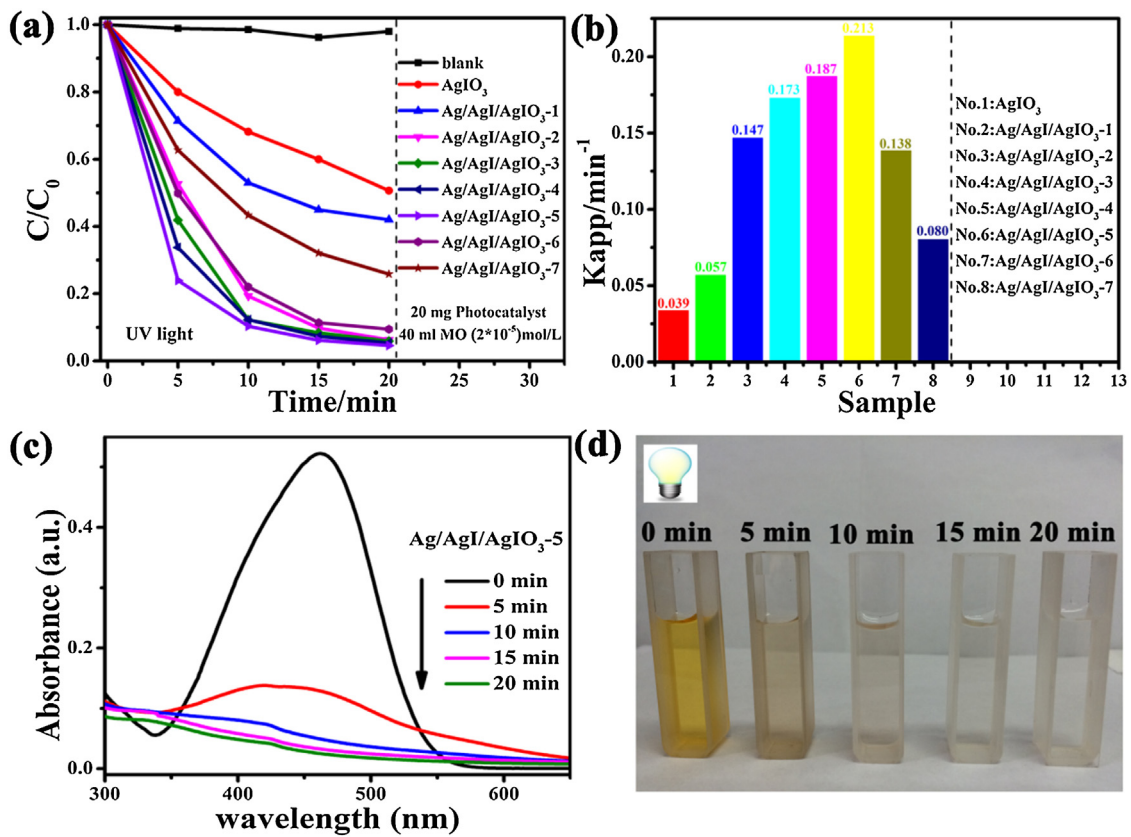


Fig. 6. Photocatalytic degradation curves of MO over the AgIO_3 precursor and Ag-AgI-AgIO_3 composite photocatalysts under UV light illumination (a), apparent rate constants for degrading MO over AgIO_3 , and Ag-AgI-AgIO_3 samples (b), temporal absorption spectra patterns (c) and color change of MO solution (d) over $\text{Ag-AgI-AgIO}_3\text{-}5$ sample (for interpretation of the references to colour in this figure legend, the reader is referred to the web version of this article).

3.3. Photocatalytic activity enhancement

3.3.1. Photodegradation of MO under visible-light irradiation

The photocatalytic performance of the as-obtained AgIO_3 precursor and Ag-AgI-AgIO_3 composite photocatalysts is first assessed by photo-disintegrating MO under visible light ($\lambda > 420 \text{ nm}$) illumination. As shown in Fig. 5(a), the blank experiment (without catalyst) exhibits that MO molecules are so stable that photolysis can be neglected. Fig. S1 displays time-resolved absorption spectra changes of MO solution over AgIO_3 , reflecting that very little MO can be degraded by AgIO_3 . All the Ag-AgI-AgIO_3 composite photocatalysts show greater photocatalytic activity than AgIO_3 precursor, which should be the synergism function of strong visible-light absorption and superior charge transfer efficiency between components in composite photocatalysts. $\text{Ag-AgI-AgIO}_3\text{-}5$ photocatalyst possesses the best photocatalytic activity than any other samples, which can remove 65.5% of MO after 40 min visible light illumination. Fig. 5(b) shows the apparent rate constants of all the as-prepared samples. The reaction kinetics of photodegrading MO in quantitative terms are determined via the pseudo-first-order equation [33]: $\ln(C_0/C) = k_{app}t$, here C , C_0 and k_{app} represent the initial MO solution concentration (mol/L), instantaneous MO solution concentration (mol/L), and rate constant (min^{-1}) at time t , respectively. With increasing the concentration of NaBH_4 , the photodegradation rate constant of Ag-AgI-AgIO_3 goes up firstly and achieves the maximum of 0.0228 min^{-1} for $\text{Ag-AgI-AgIO}_3\text{-}5$ sample, which is 15.2 and 2.89 times higher than those of pure AgIO_3 (0.0015 min^{-1}) and $\text{Ag-AgI-AgIO}_3\text{-}7$ (0.0079 min^{-1}) sample, and then declines with further increasing NaBH_4 concentration. Temporal absorption spectra patterns of MO over $\text{Ag-AgI-AgIO}_3\text{-}5$ sample are shown in Fig. 5(c). One can see the absorbance of MO solution is gradually dimin-

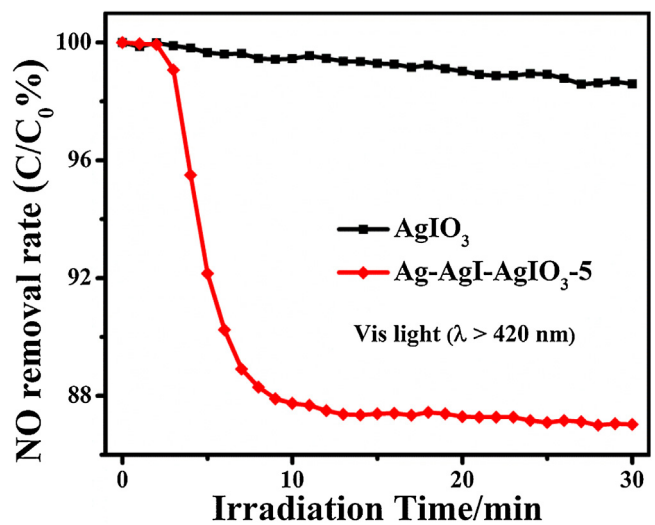


Fig. 7. Photocatalytic removal gaseous NO under visible light illumination ($\lambda > 420 \text{ nm}$).

ished under visible light irradiation. Simultaneously, the color of MO solution is also shallowed, as shown in Fig. 5(d).

3.3.2. Photodegradation of MO under UV irradiation

As AgIO_3 is primarily activated by UV light, we also explore the photocatalytic activity of as-synthesized composite photocatalysts under excitation of UV light. As displayed in Fig. 6(a), almost no MO can be degraded in the absence of photocatalyst. Fig. S2 shows time-resolved spectra changes of MO over AgIO_3 . The pho-

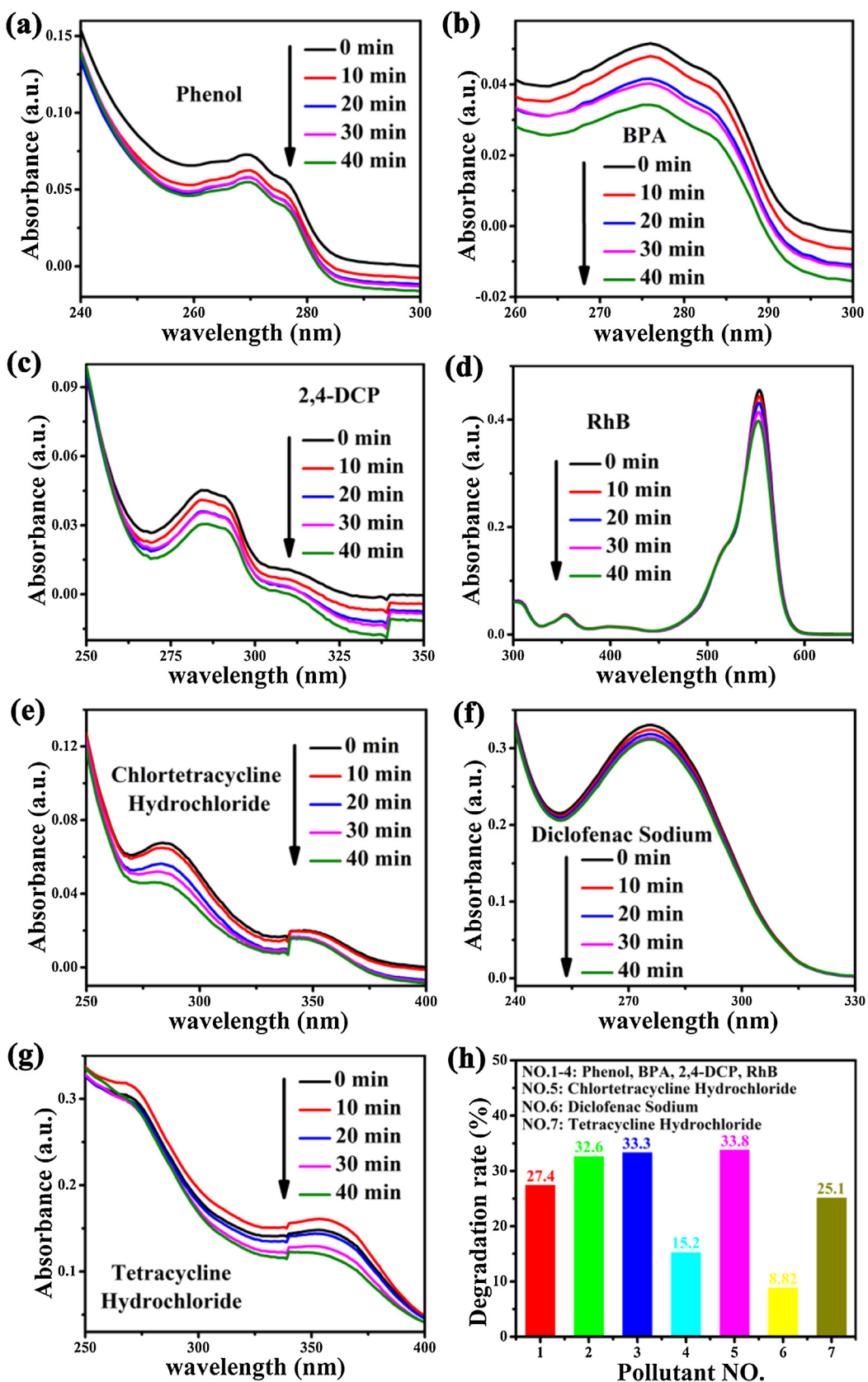


Fig. 8. Temporal absorption spectra of Phenol (a), BPA (b), 2,4-DCP (c), RhB (d), chlortetracycline hydrochloride (e), diclofenac sodium (f), tetracycline hydrochloride (g) over Ag-AgI-AgI_{0.5}-5 composite photocatalyst under visible light ($\lambda > 420$ nm) irradiation. Degradation rate of multiple contaminants after 40 min visible light irradiation (h).

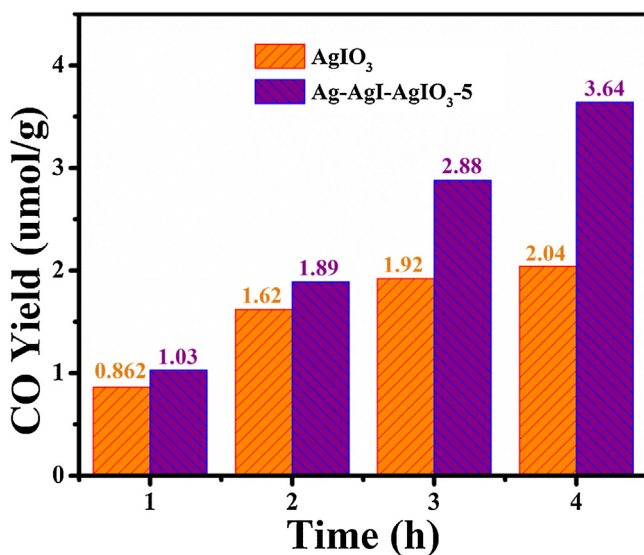


Fig. 9. Time dependence of CO yields over pure AgIO₃ and Ag-AgI-AgIO₃-5 samples under simulated solar light irradiation.

tocatalytic activities of Ag-AgI-AgIO₃ composite photocatalysts are also superior to the pristine AgIO₃. Particularly, Ag-AgI-AgIO₃-5 still exhibits the highest decomposition efficiency among all the samples, which can remove 95.4% of MO after 40 min UV light irradiation. The apparent rate constants of all the samples are exhibited in Fig. 6(b). The photodegradation rate constant of Ag-AgI-AgIO₃-5 sample is 0.213 min⁻¹, which reaches 5.46 and 2.66 times higher than those of AgIO₃ (0.039 min⁻¹) and Ag-AgI-AgIO₃-7 (0.08 min⁻¹). According to Fig. 6(c) and (d), with prolonging the time of UV light irradiation, the concentration of MO solution is continuously decreased and its color also shallows.

3.3.3. Photodegradation of NO

NO, as reported in previous papers [34], cannot be photolyzed without photocatalytic materials. In the presence of photocatalyst, NO can reacts with photoinduced reactive radicals and produce HNO₂ or HNO₃ as the final products [35]. Herein, we evaluate the photocatalytic activity of AgIO₃ and Ag-AgI-AgIO₃-5 via removing NO in air under visible light ($\lambda > 420$ nm) irradiation. It can be observed from Fig. 7 that AgIO₃ remove a slight of NO (<2%). However, Ag-AgI-AgIO₃-5 composite photocatalyst can remove 12.9% of NO after 30 min visible light irradiation, reflecting the positive effects of heterojunction and SPR effect of Ag particles.

3.3.4. Photodegradation of diverse pollutants

To further study the universality of Ag-AgI-AgIO₃-5 composite photocatalyst, diverse industrial pollutants, including BPA, 2,4-DCP, phenol, RhB, and pharmaceuticals like chlortetracycline hydrochloride, diclofenac sodium, tetracycline hydrochloride are used as target contaminants. These pollutants and pharmaceuticals can cause tissue necrosis or reproductive abnormalities for human health [36]. Fig. 8(a–g) display temporal absorption spectra of phenol, BPA, 2,4-DCP, RhB, chlortetracycline hydrochloride, diclofenac sodium, and tetracycline hydrochloride over Ag-AgI-AgIO₃-5 under visible light ($\lambda > 420$ nm) irradiation. What is amazing is that Ag-AgI-AgIO₃-5 can decompose all the above-mentioned pollutants. Removal efficiencies reach 27.4%, 32.6%, 33.3%, 15.2%, 33.8%, 8.82%, and 25.1% for phenol, BPA, 2,4-DCP, RhB, chlortetracycline hydrochloride, diclofenac sodium, and tetracycline hydrochloride, respectively. These observations reflect the universally strong photooxidation ability of the Ag-AgI-AgIO₃-5 composite photocatalyst.

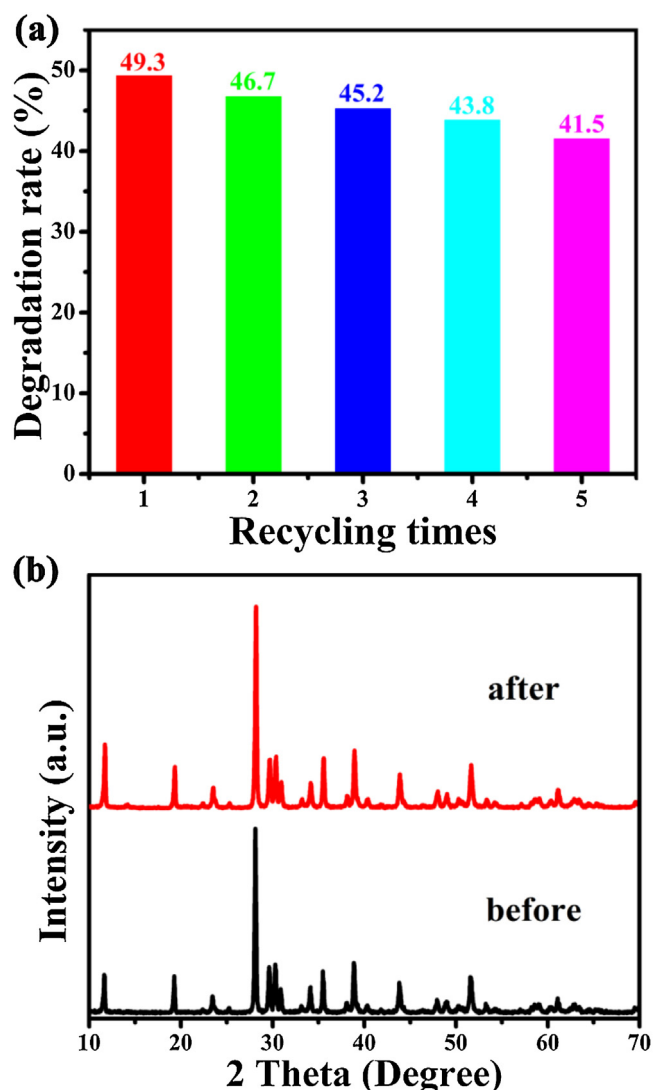


Fig. 10. Cycling runs for photo-degrading MO (a) and XRD pattern (b) before and after photocatalysis for Ag-AgI-AgIO₃-4 composite photocatalyst.

3.3.5. Photoreducing CO₂ to CO

CO₂ is the main cause of the greenhouse effect. Nowadays, photocatalytic technology for converting CO₂ to be CO, CH₄ or other renewable energy using renewable solar energy attracts tremendous attention because it can settle both greenhouse effect and energy crisis at the same time. Accordingly, CO₂ reduction experiments over pure AgIO₃ and Ag-AgI-AgIO₃-5 samples are carried out, as shown in Fig. 9. The CO₂ reduction occurs in the presence of AgIO₃ precursor or Ag-AgI-AgIO₃-5 composite photocatalyst. But the photocatalytic activity of AgIO₃ is weaker than Ag-AgI-AgIO₃-5. The generation of CO over AgIO₃ and Ag-AgI-AgIO₃-5 is 2.04 umol/g and 3.64 umol/g, respectively. These results confirm the significant role of heterostructure and SPR effect of Ag species.

3.3.6. Stability of photocatalyst

Five-cycle recycling experiments are carried out to investigate the stability of the as-obtained photocatalysts, which is another important consideration for their practical application except for photocatalytic activity. As shown in Fig. 10(a), there is just a slight decline in photocatalytic activity after five successive cycles. In addition, the XRD pattern almost does not change after photoreaction while comparing with the XRD pattern before photoreaction (Fig. 10(b)). These results manifest the high stability of

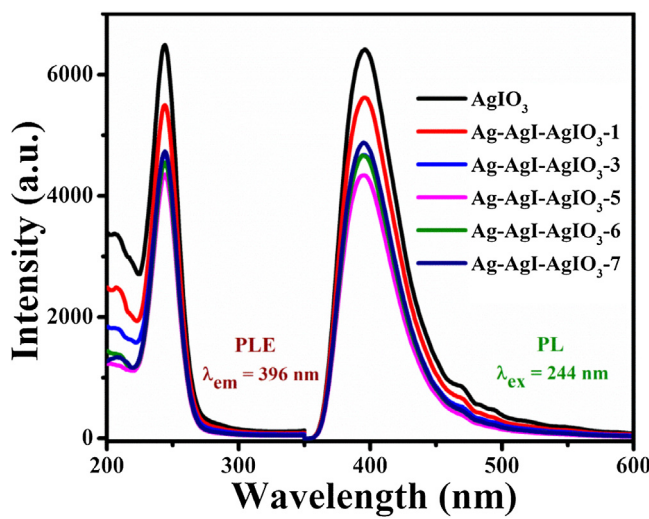


Fig. 11. The photoluminescence excitation (PLE) spectra and photoluminescence emission (PL) spectra of pure AgIO_3 and Ag-AgI-AgIO_3 composite photocatalysts.

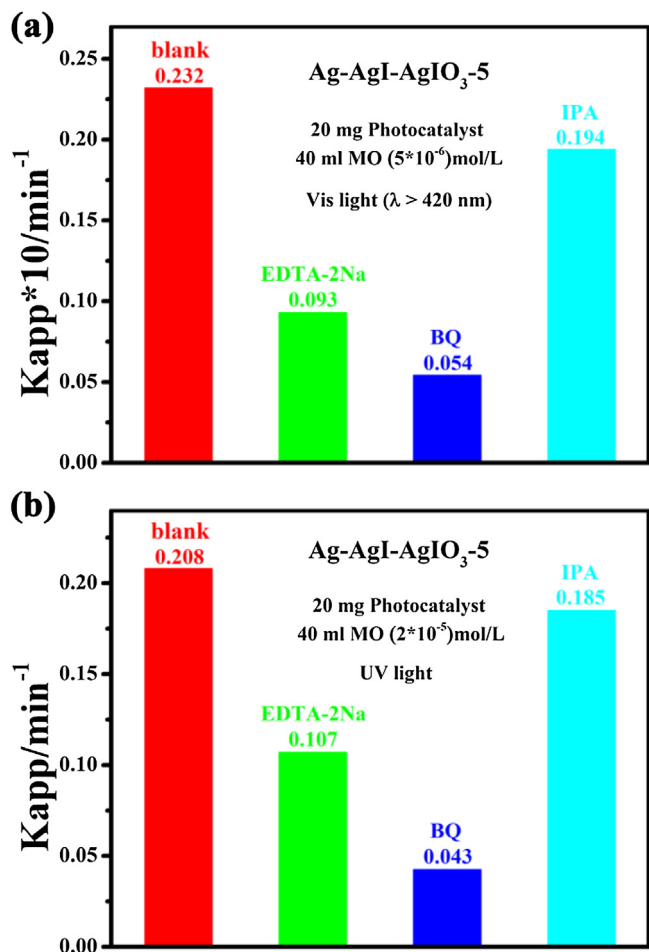


Fig. 12. Photocatalytic degradation of MO over Ag-AgI-AgIO_3 -5 composite photocatalysts alone and with different scavengers under irradiation of visible light ($\lambda > 420 \text{ nm}$) (a) and UV light (b).

Ag-AgI-AgIO_3 -4 composite photocatalyst, boding for its promising applications in environmental remediation.

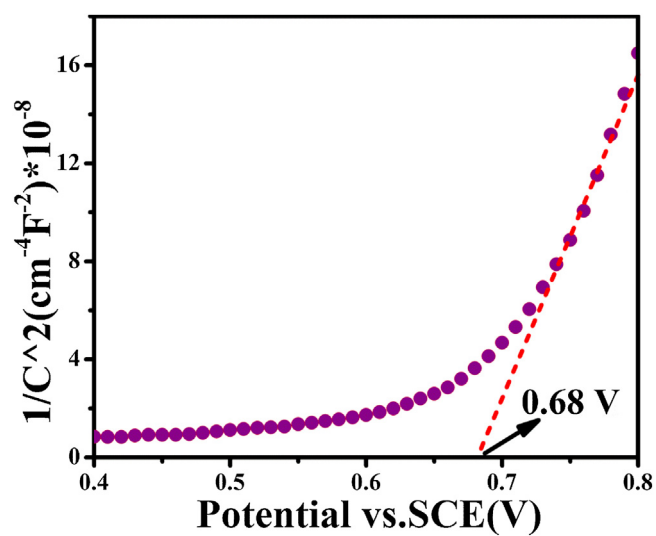


Fig. 13. Mott–Schottky curve of AgIO_3 photocatalyst.

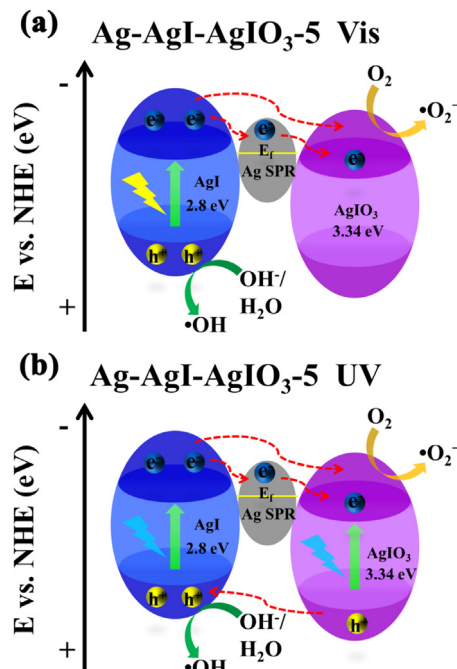


Fig. 14. The proposed photocatalytic mechanisms scheme over Ag-AgI-AgIO_3 -5 composite photocatalyst under irradiation of visible light (a) and UV light (b).

3.4. Charge separation and photocatalytic enhancement mechanism

To our knowledge, the recombination efficiency of photoinduced charge carrier is crucial to photocatalytic activity of photocatalyst [37]. Fortunately, the photoluminescence emission spectra can provide direct evidence for the recombination rate of photogenerated holes and electrons [38]. The photoluminescence excitation (PLE) spectra and photoluminescence emission (PL) spectra of pure AgIO_3 and Ag-AgI-AgIO_3 composite photocatalysts are shown in Fig. 11. Emission intensity of AgIO_3 precursor is higher than that of Ag-AgI-AgIO_3 composite photocatalysts around 396 nm. Particularly, Ag-AgI-AgIO_3 -5 sample exhibits the lowest intensity among all the samples, reflecting its possibly best photocatalytic activity. This is in accordance with the results of MO photodegradation experiments. Thus, it is believed that fabrica-

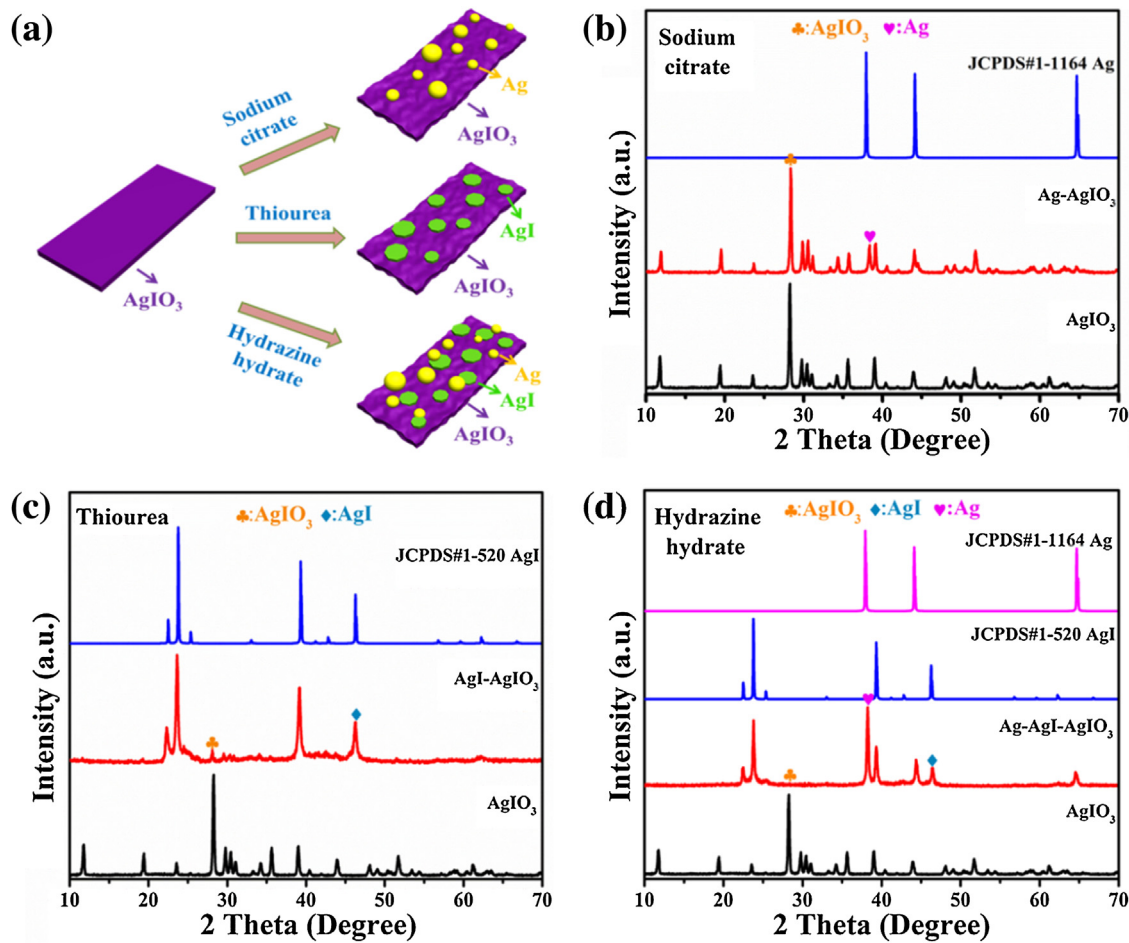


Fig. 15. Schematic illustration of morphology change for products from the redox reaction between pure AgIO₃ and different reductants (a), XRD patterns for products of AgIO₃ precursor reacting with sodium citrate (b), thiourea (c), and hydrazine hydrate (d).

tion of heterostructure can effectively inhibit the recombination of photoexcited e⁻-h⁺ pairs, and greatly improve photocatalytic performance for composite photocatalyst.

To identify the main active species for photodegrading MO, active species trapping experiments are conducted with adding disodium ethylenediaminetetraacetate (EDTA-2Na), isopropanol (IPA), and benzoquinone (BQ) to quench h⁺, •OH, and •O₂⁻, respectively [39]. As shown in Fig. 12(a-b), under irradiation of visible light or UV light, the addition of both BQ and EDTA-2Na can greatly decreases the MO photodegradation rate constant, and IPA has a slight effect. This phenomenon demonstrated that the crucial active species of Ag-AgI-AgIO₃ composite photocatalyst are •O₂⁻ and h⁺ regardless of UV or visible light irradiation.

To identify the band structure of pure AgIO₃ photocatalyst, Mott-Schottky method is employed. The flat-band potential value (E_{fb}) is determined by the following Mott-Schottky equation [40].

$$\frac{1}{C^2} = \frac{2}{\varepsilon \varepsilon_0 N_D} \left(E - E_{fb} - \frac{k_B T}{q} \right)$$

Here ε are ε_0 the dielectric constants of free space and the film electrode, and C , κ_b , E , T , N_D , and q means the space charge capacitance, Boltzmann's constant, applied potential, temperature, donor density, and electronic charge, respectively. By intercepting the extrapolation to $1/C^2 = 0$ (Fig. 13), the flat potential (E_{fb}) of AgIO₃ is calculated to be 0.68 V versus saturated calomel electrode (SCE), which is equal to 0.92 V versus the normal hydrogen electrode (NHE). AgIO₃ is deemed as an *n*-type semiconductor due to the positive slop of Mott-Schottky curve. On the basis of previous paper

[41], for an *n*-type semiconductor, the flat potential is 0.1–0.3 eV lower than the conduction band position, depending on the carrier concentration and electron effective mass. Accordingly, the conduction band (CB) of AgIO₃ is 0.62 eV, and its valence band (VB) is 3.96 eV.

Based on the band structure, proposed photocatalytic mechanisms over the Ag-AgI-AgIO₃-5 composite photocatalyst under visible and UV light irradiation are schematically exhibited in Fig. 14. It can be inferred from previous paper that the CB and VB of AgI with a relatively narrow band gap (2.8 eV) are -0.15 eV and 2.65 eV, respectively [42]. Under the illumination of visible light (Fig. 14(a)), electrons and hole can be produced on AgI. AgI₃ cannot absorb visible light due to its wide band gap (3.34 eV). Because of the Ag SPR effect, the photoinduced electrons can be excited from its Fermi level (0.4 eV) [43,44]. The CB of AgI (-0.15 eV) is higher than the Fermi level of Ag (0.4 eV) and CB of AgIO₃ (0.62 eV). Thus, photo-generated electrons of AgI transfer to Ag nanoparticles and the CB of AgIO₃. Meantime, electrons of metallic Ag also transfer to the CB of AgIO₃. In theory, the electrons on the CB of AgIO₃ cannot reduce O₂ to produce •O₂⁻, because the more positive CB potential of AgIO₃ (0.61 eV) compared to O₂/•O₂⁻ (-0.05 eV) [36]. However, as shown in Fig. 9, both pure AgIO₃ and Ag-AgI-AgIO₃-5 photocatalyst can reduce CO₂ to CO. The redox potentials of CO₂/CO is -0.53 eV [22], which is more negative than CB of AgIO₃ (0.61 eV) and O₂/•O₂⁻ (-0.05 eV). It can be deduced that, in actual photocatalytic system, The AgIO₃ fermi level would shift to rearrange the energy level and surrounding medium for AgIO₃. Thereby, electrons on CB of AgIO₃ can reduce O₂ to •O₂⁻ in actual photocat-

alytic system, which matches well with the results of active species trapping experiments. On the other hand, the VB of AgI is 2.65 eV, which is more positive than the potentials of $\bullet\text{OH}/\text{OH}^-$ (1.99 eV) and $\bullet\text{OH}/\text{H}_2\text{O}$ (2.27 eV) [36], so the holes on the VB of AgI can oxidize OH^- to $\bullet\text{OH}$. Under the irradiation of UV light (Fig. 14(b)), AgIO_3 also can be excited and produce electron-hole pairs. Electrons of AgI and metallic Ag would transfer to the CB of AgIO_3 , and electrons would reduce O_2 to $\bullet\text{O}_2^-$. Holes of AgIO_3 would transfer VB of AgI, and holes oxidize OH^- to $\bullet\text{OH}$. No matter what kind of excitation light source we use, the gaseous NO can be oxidized by $\bullet\text{O}_2^-$, $\bullet\text{OH}$, and h^+ to the final products as HNO_2 and HNO_3 [35,45]. Moreover, the CO_2 gas is reduced by e^- to CO [46].

3.5. Exploring the reduction products of AgIO_3 by other reductants

Besides, we also explore the reduction products of AgIO_3 by other reductants, such as sodium citrate, thiourea, and hydrazine hydrate. Fascinatingly, different reductants result in distinct reduction products (Fig. 15(a)). The XRD patterns of products for AgIO_3 precursor reacting with the above-mentioned reductants are shown in Fig. 15(b-d). Ag-AgI-AgI O_3 ternary photocatalyst can also be gotten by using hydrazine hydrate to reduce AgIO_3 (Fig. 15(d)). However, taking sodium citrate and thiourea as reductants separately produce Ag-AgI O_3 (Fig. 15(b)) and AgI-AgI O_3 (Fig. 15(c)) composite photocatalysts. These diverse phenomena demonstrated that the reduction on redox-couple containing photocatalyst is a promising way to prepare multiple-components photocatalytic materials.

4. Conclusions

On the basis of redox couples Ag/Ag^+ and $\text{I}^-/(\text{IO}_3)^-$ in AgIO_3 , several kinds of multiplex heterostructure photocatalysts, including Ag-AgI O_3 , AgI-AgI O_3 and Ag-AgI-AgI O_3 , are synthesized by a facile in-situ reduction reaction taking AgIO_3 as a self-sacrificed template. Among them, Ag-AgI-AgI O_3 ternary composite photocatalysts obtained through the reduction reaction between AgIO_3 and NaBH_4 are systematically studied in this article. Compared to the AgIO_3 precursor, the light absorption and photocatalytic activity of Ag-AgI-AgI O_3 composite photocatalysts are greatly enhanced. The Ag-AgI-AgI O_3 -5 composite photocatalyst shows the best photocatalytic performance for photodegrading methyl orange (MO) under visible or UV light illumination, and more importantly Ag-AgI-AgI O_3 -5 sample can also effectively photodegrade diverse industrial contaminants and pharmaceuticals, such as RhB, BPA, 2,4-DCP, phenol, chlortetracycline hydrochloride, tetracycline hydrochloride, diclofenac sodium and even NO gas under visible light ($\lambda > 420$ nm) irradiation. Notably, Ag-AgI-AgI O_3 -5 exhibits improved photocatalytic performance in converting CO_2 to CO. The photocatalytic mechanisms of Ag-AgI-AgI O_3 -5 ternary photocatalyst corresponding to different light sources are studied in detail. These findings provide new insight into designing multiple heterojunctional photocatalysts with high-performance via a facile one-step strategy.

Acknowledgements

This work is supported by the National Natural Science Foundations of China (Grant No. 51302251 and 51372233), the Fundamental Research Funds for the Central Universities (No. 2652015296).

Appendix A. Supplementary data

Supplementary data associated with this article can be found, in the online version, at <http://dx.doi.org/10.1016/j.apcatb.2016.07.029>.

References

- [1] Y.H. Zhang, Z.R. Tang, X.Z. Fu, Y.J. Xu, *Appl. Catal. B-Environ.* 106 (2011) 445–452.
- [2] Z.Y. Zhang, Y.Z. Huang, K.C. Liu, L.J. Guo, Q. Yuan, B. Dong, *Adv. Mater.* 27 (2015) 5906–5914.
- [3] S.M. Wang, D.L. Li, C. Sun, S.G. Yang, Y. Guan, H. He, *Appl. Catal. B-Environ.* 144 (2014) 885–892.
- [4] S.A. Ansari, M.M. Khan, M.O. Ansari, J. Lee, M.H. Cho, *J. Phys. Chem. C* 117 (2013) 27023–27030.
- [5] Y.Z. Li, H. Zhang, Z.M. Guo, J.J. Han, X.J. Zhao, Q.N. Zhao, S.J. Kim, *Langmuir* 24 (2008) 8351–8357.
- [6] K. Zhang, D.Q. Zhang, J. Liu, K.X. Ren, H. Luo, Y.J. Peng, G.S. Li, X.B. Yu, *CrystEngComm* 14 (2012) 700–707.
- [7] H.D. Zang, P.K. Routh, Y. Huang, J.S. Chen, E. Sutter, P. Sutter, M. Cotlet, *ACS Nano* 10 (2016) 4790–4796.
- [8] X.B. Wei, C.L. Shao, X.H. Li, N. Lu, K.X. Wang, Z.Y. Zhang, Y.C. Liu, *Nanoscale* 8 (2016) 11034–11043.
- [9] M.C. Long, P.D. Hu, H.D. Wu, J. Cai, B.H. Tan, B.X. Zhou, *Appl. Catal. B-Environ.* 184 (2016) 20–27.
- [10] L. Sun, R.Z. Zhang, Y. Wang, W. Chen, *ACS Appl. Mater. Interfaces* 6 (2014) 14819–14826.
- [11] Y. Sang, L. Kuai, C.Y. Chen, Z. Fang, B.Y. Geng, *ACS Appl. Mater. Interfaces* 6 (2014) 5061–5068.
- [12] Q. Zhu, W.S. Wang, L. Lin, G.Q. Gao, H.L. Guo, H. Du, A.W. Xu, *J. Phys. Chem. C* 117 (2013) 5894–5900.
- [13] X.F. Yang, Z.P. Chen, J.S. Xu, H. Tang, K.M. Chen, Y. Jiang, *ACS Appl. Mater. Interfaces* 7 (2015) 15285–15293.
- [14] H.F. Li, H.T. Yu, X. Quan, S. Chen, Y.B. Zhang, *ACS Appl. Mater. Interfaces* 8 (2016) 2111–2119.
- [15] H.L. Wang, L.S. Zhang, Z.G. Chen, J.Q. Hu, S.J. Li, Z.H. Wang, J.S. Liu, X.C. Wang, *Chem. Soc. Rev.* 43 (2014) 5234–5244.
- [16] P. Zhou, J.G. Yu, M. Jaroniec, *Adv. Mater.* 26 (2014) 4920–4935.
- [17] W.J. Wang, H.F. Cheng, B.B. Huang, X.R. Li, X.Y. Qin, X.Y. Zhang, Y. Dai, *Inorg. Chem.* 53 (2014) 4989–4993.
- [18] H.W. Huang, Y. He, R. He, Z.S. Lin, Y.H. Zhang, S.C. Wang, *Inorg. Chem.* 53 (2014) 8114–8119.
- [19] X.M. Qi, M.L. Gu, X.Y. Zhu, J. Wu, H.M. Long, K. He, Q. Wu, *Chem. Eng. J.* 285 (2016) 11–19.
- [20] Z.Z. Lou, B.B. Huang, Z.Y. Wang, X.C. Ma, R. Zhang, X.Y. Zhang, X.Y. Qin, Y. Dai, M.H. Whangbo, *Chem. Mater.* 26 (2014) 3873–3875.
- [21] H.W. Huang, Y. He, Y.X. Guo, R. He, Z.S. Lin, Y.H. Zhang, *Solid State Sci.* 46 (2015) 37–42.
- [22] Z.Q. He, D. Wang, H.Y. Fang, J.M. Chen, S. Song, *Nanoscale* 6 (2014) 10540–10544.
- [23] Y.S. Lee, H.J. Lee, W.S. Choi, *Langmuir* 30 (2014) 9584–9590.
- [24] G.Q. Luo, X.J. Jiang, M.J. Li, Q. Shen, L.M. Zhang, H.G. Yu, *ACS Appl. Mater. Interfaces* 5 (2013) 2161–2168.
- [25] C. Hu, J. Guo, J.H. Qu, X.X. Hu, *Langmuir* 23 (2007) 4982–4987.
- [26] Y.C. Yang, J.W. Wen, J.H. Wei, R. Xiong, J. Shi, C.X. Pan, *ACS Appl. Mater. Interfaces* 5 (2013) 6201–6207.
- [27] J. Jiang, L.Z. Zhang, H. Li, W.W. He, J.J. Yin, *Nanoscale* 5 (2013) 10573–10581.
- [28] C. Zeng, Y.M. Hu, Y.X. Guo, T.R. Zhang, F. Dong, X. Du, Y.H. Zhang, H.W. Huang, *Appl. Catal. B: Environ.* 194 (2016) 62–73.
- [29] X.F. Yang, Z.P. Chen, J.S. Xu, H. Tang, K.M. Chen, Y. Jiang, *ACS Appl. Mater. Interfaces* 7 (2015) 15285–15293.
- [30] Y.Y. Bu, Z.Y. Chen, *ACS Appl. Mater. Interfaces* 6 (2014) 17589–17598.
- [31] X. Xiao, C.L. Xing, G.P. Hea, X.X. Zuo, J.M. Nan, L.S. Wang, *Appl. Catal. B-Environ.* 148 (2014) 154–163.
- [32] R. Qiao, M.M. Mao, E.L. Hu, Y.J. Zhong, J.Q. Ning, Y. Hu, *Inorg. Chem.* 54 (2015) 9033–9039.
- [33] C.Y. Liu, H.W. Huang, X. Du, T.R. Zhang, N. Tian, Y.X. Guo, Y.H. Zhang, *J. Phys. Chem. C* 119 (2015) 17156–17165.
- [34] F. Dong, Z.W. Zhao, T. Xiong, Z.L. Ni, W.D. Zhang, Y.J. Sun, W.K. Ho, *ACS Appl. Mater. Interfaces* 5 (2013) 11392–11401.
- [35] F. Dong, Q.Y. Li, Y.J. Sun, W.K. Ho, *ACS Catal.* 4 (2014) 4341–4350.
- [36] H.W. Huang, Y. He, X.W. Li, M. Li, C. Zeng, F. Dong, X. Du, T.R. Zhang, Y.H. Zhang, *J. Mater. Chem. A* 3 (2015) 24547–24556.
- [37] H.W. Huang, X.W. Li, J.J. Wang, F. Dong, P.K. Chu, T.R. Zhang, Y.H. Zhang, *ACS Catal.* 5 (2015) 4094–4103.
- [38] S.X. Weng, J. Hu, M.L. Lu, X.X. Ye, Z.X. Pei, M. Huang, L.Y. Xie, S. Lin, P. Liu, *Appl. Catal. B-Environ.* 163 (2015) 205–213.
- [39] Y.X. Guo, H.W. Huang, Y. He, N. Tian, T.R. Zhang, P.K. Chu, Q. An, Y.H. Zhang, *Nanoscale* 7 (2015) 11702–11711.
- [40] H.W. Huang, K. Xiao, K. Liu, S.X. Yu, Y.H. Zhang, *Cryst. Growth Des.* 16 (2016) 221–228.

[41] N. Tian, H.W. Huang, C.Y. Liu, F. Dong, T.R. Zhang, X. Du, S.X. Yu, Y.H. Zhang, *J. Mater. Chem. A* 3 (2015) 17120–17129.

[42] Y.P. Bi, S.X. Ouyang, J.Y. Cao, J.H. Ye, *Phys. Chem. Chem. Phys.* 13 (2011) 10071–10075.

[43] F. Dong, Q.Y. Li, Ying. Zhou, Y.J. Sun, H.D. Zhang, Z.B. Wu, *Dalton Trans.* 43 (2014) 9468–9480.

[44] C. Zeng, Y.M. Hu, Y.X. Guo, T.R. Zhang, F. Dong, Y.H. Zhang, H.W. Huang, *ACS Sustainable Chem. Eng.* 4 (2016) 3305–3315.

[45] F. Dong, Z.W. Zhao, Y.J. Sun, Y.X. Zhang, S. Yan, Z.B. Wu, *Environ. Sci. Technol.* 49 (2015) 12432–12440.

[46] L.Q. Ye, X.L. Jin, X.X. Ji, C. Liu, Y.R. Su, H.Q. Xie, C. Liu, *Chem. Eng. J.* 291 (2016) 39–46.